Neuroradiology (2004) 46: 130–135
DOI 10.1007/s00234-003-1152-4

T. Takeguchi
H. Miki
T. Shimizu
K. Kikuchi
T. Mochizuki
S. Ohue
T. Ohnishi

The dural tail of intracranial meningiomas on fluid-attenuated inversion-recovery images

Received: 6 October 2003
Accepted: 17 November 2003
Published online: 28 January 2004

T. Takeguchi (✉) · H. Miki
T. Shimizu · K. Kikuchi · T. Mochizuki
Department of Radiology,
Ehime University School of Medicine,
Shitsukawa, Shigenobucho,
Onsengun, 791-0295, Onsengun Ehime,
Japan
E-mail: takegu@m.ehime-u.ac.jp
Tel.: +81-89-9605371
Fax: +81-89-9605375

S. Ohue · T. Ohnishi
Department of Neurosurgery,
Ehime University School of Medicine,
Shitsukawa, Shigenobucho, Onsengun,
791-0295 Ehime, Japan

Abstract We evaluated the "dural tail" associated with 48 intracranial meningiomas on fluid-attenuated inversion-recovery (FLAIR) and contrast-enhanced T1-weighted images. In 30 (62.5%), a dural tail was observed on contrast-enhanced T1-weighted images, and thickening of the dura mater and abnormal signal were identified in the corresponding region on FLAIR images. Thus, FLAIR imaging was useful for showing dural abnormality associated with meningiomas without the needed for contrast medium.

Keywords Meningioma · Dural tail · Magnetic resonance imaging

Introduction

Linear thickening and contrast enhancement along the dura mater adjacent to meningiomas has been called a "dural tail", "meningeal tail", or "meningeal flare" [1, 2, 3, 4, 5, 6]. Its reported frequency with meningiomas ranges from 52 to 72% on MRI [5, 6, 7, 8]. It is generally assessed on contrast-enhanced T1-weighted images [3, 7, 9].

Images obtained by fluid-attenuated inversion-recovery (FLAIR) sequences, which have become widely used in clinical practice, are T2-weighted images on which cerebrospinal fluid (CSF) signals have been suppressed [10, 11]. FLAIR is useful for imaging high-signal lesions adjacent to CSF. Therefore, we considered that a dural tail, which indicates abnormalities of the dura mater adjacent to CSF should be detectable on FLAIR images. We hypothesised that abnormal signal corresponding to the dural tail which had been masked by high signal from CSF, could be seen after suppressing the CSF signal. To our knowledge, there has been no report on the dural tail on FLAIR images.

Materials and methods

We retrospectively examined the MRI findings of 48 intracranial meningiomas in 46 patients, in whom T1-weighted inversion recovery (IR), T2-weighted turbo spin-echo (TSE), turbo FLAIR, and contrast-enhanced T1-weighted IR images were obtained during one examination in our hospital. There were 13 men and 33 women 26–77 years (mean 53.9 years) of age. In eight cases the diagnosis of meningioma was clinical, but 40 were treated surgically and histologically proven. We excluded intraventricular meningiomas.

MRI was performed at 1.5 tesla using a circular head coil. All images were acquired at the same levels. Imaging parameters were as follows. T2-weighted TSE: TR 4263 effective TE 110 ms,

echo-train length 10, matrix 247×512, field of view 220 mm, section thickness 6 mm, intersection gap 0.6 mm, two acquisitions, imaging time 2 min 54 s; FLAIR: TR 6000 effective TE 150 TI 2000 ms, echo-train length 23, matrix 193×512, field of view 220 mm, section thickness 6 mm, intersection gap 0.6 mm, two acquisitions, imaging time 3 min; T1-weighted IR: TR 2000 TE 10, TI 860 ms, echo-train length 6, matrix 203×512, field of view 220 mm, section thickness 6 mm, intersection gap 0.6 mm, two acquisitions, imaging time 3 min 20 s.

We first determined whether a dural tail seen on contrast enhanced T1-weighted IR images, and noted the relationship between the presence of a dural tail and the site of the tumour. Where a dural tail was present, its degree of enhancement was classified into as, weak, equal, moderate and strong, according to the difference between the tail and the parenchyma of the tumour. Then, in the patients with a dural tail, we examined the signal pattern on FLAIR images, comparing it with the parenchyma of the tumour, and classifying it as lower, isointense, and slightly or markedly more intense. Two neuroradiologists performed the grading by consensus.

In five of the surgical cases, abnormal dura mater corresponding to the dural tail was resected. Infiltration of tumour cells and the changes in the reactivity were assessed pathologically and compared to the MRI findings.

Results

The tumours ranged in size from 2.0 to 8.5 cm (mean 3.8 cm). They lay on the falx cerebri (in nine cases), sphenoid ridge (nine), convexity (eight), clivus (five), parasagittal region (five), cerebellopontine angle (four), tentorium (three), tuberculum sellae (three) and olfactory groove (two). Of the surgically treated cases 24 were meningotheliomatous, five angiomatous, four transitional, four atypical, two psammomatous and one was plasmocyte-rich.

A dural tail was observed on contrast-enhanced T1-weighted IR images in 30 cases (62.5%). Table 1 shows the relationship between the presence of a dural tail and tumour site. All nine patients with a falx meningioma showed a dural tail, while in the patients with parasagittal and tuberculum sellae tumours, the proportion was relatively low: 2/5 (40.0%) and 1/3 (33.3%), respectively.

Table 1 Dural tails and tumour site in 30 cases

Site	Imaging sequence	
	Contrast-enhanced T1-weighted inversion recovery	Fluid-attenuated inversion-recovery
Falx cerebri	9/9 (100%)	9/9 (100%)
Sphenoid ridge	5/9 (55.6)	5/9 (55.6)
Convexity	5/8 (62.5)	5/8 (62.5)
Parasagittal	2/5 (40.0)	2/5 (40.0)
Clivus	3/5 (60.0)	3/5 (60.0)
Cerebellopontine angle	2/4 (50.0)	2/4 (50.0)
Tentorium	2/3 (66.7)	2/3 (66.7)
Tuberculum sellae	1/3 (33.3)	1/3 (33.3)
Olfactory groove	1/2 (50.0)	1/2 (50.0)

Table 2 Degree of contrast enhancement of the dural tail compared to the meningioma on contrast-enhanced T1-weighted inversion recovery images in 30 cases

Enhancement	Weak	Equal	Moderately increased	Markedly increased
Cases (%)	0 (0)	9 (30.0)	10 (33.3)	11 (36.7)

Table 2 shows the degree of contrast enhancement of the dural tail.

Hypertrophy of the dura mater and abnormal signal were observed on FLAIR images in all 30 lesions with a dural tail (Table 1, Fig 1). Table 3 shows the signal intensity in the dura mater corresponding to the dural tail.

In four of the five cases examined histologically the dura mater corresponding to the tail was infiltrated by tumour cells; in all these patients the tail was seen on MRI (Fig. 2). In other patient there were no tumour cells in the dural tail, but the vascular lumina were dilated (Fig. 3). Table 4 shows the signal intensity of the dural tail on contrast-enhanced T1-weighted and FLAIR images in these patients.

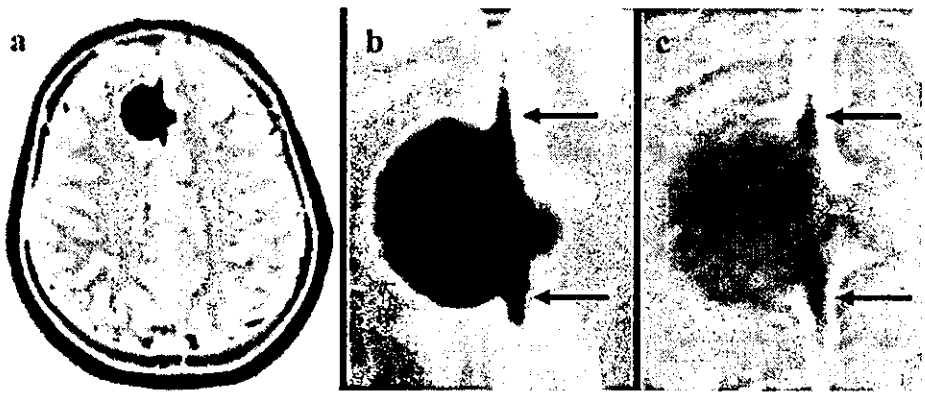

Fig. 1a–c A 49-year-old woman with a falx meningioma **a, b** A dural tail is seen on contrast-enhanced T1-weighted inversion-recovery (IR) images (*arrows*). **c** Hypertrophy of the dura mater and abnormal high signal are identified in this region on a fast fluid-attenuated inversion recovery (FLAIR) image (*arrows*)

Table 3 Signal intensity of the dural tail compared to the meningioma on fluid-attenuated inversion-recovery (FLAIR) images in 30 cases

Signal	Low	Isointense	Slightly increased	Markedly increased
Cases (%)	0 (0)	12 (40.0)	11 (36.7)	7 (23.3)

Discussion

A flat, contrast-enhancing structure, probably dural, is seen on contrast-enhanced T1-weighted images in 52–72% of meningiomas [5, 6, 7, 8]; this range is consistent with our finding of 62.5%. However, there are differences between regions, possibly because the examinations were performed only in the axial plane we use for routine imaging. If imaging had included other planes of sections, the rates might have been higher.

Goldsher et al. [7] reported thickening and enhancement of the dura mater extending away from the tumour in 18 of 30 intracranial meningiomas (60%) and considered it highly specific or at least strongly supportive of the diagnosis of meningioma. Subsequently, a dural tail has also been reported with other lesions including glioma, vestibular schwannoma, lymphoma, metastasis, adenoid cystic carcinoma, sarcoidosis and aneurysm [1, 2, 3, 4, 12, 13, 14]. It thus appears to be highly suggestive but not specific.

There have been a number of studies of the application of FLAIR imaging to brain diseases, emphasising its usefulness [15, 16, 17]. Since CSF signals are suppressed on FLAIR images, they are useful for showing lesions adjacent to the surface of the brain and the

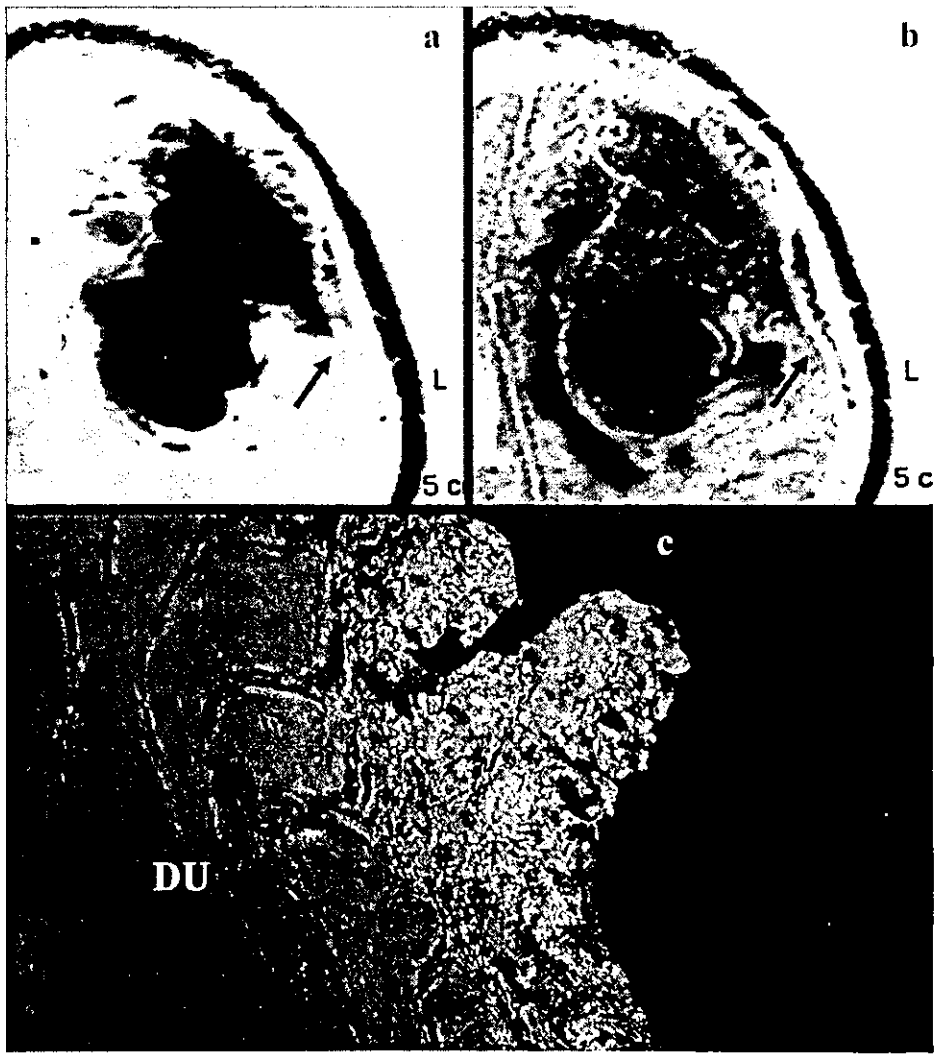

Fig. 2a–c A 48-year-old woman with a left convexity meningioma. a A dural tail tapers away from the point of attachment of the tumour to the dura mater (*arrow*). b Its signal intensity on a FLAIR image is isointense with that of the tumour. c A photomicrograph shows that clusters of meningeal cells (*) are implanted on the surface of the dura mater (*DU*)

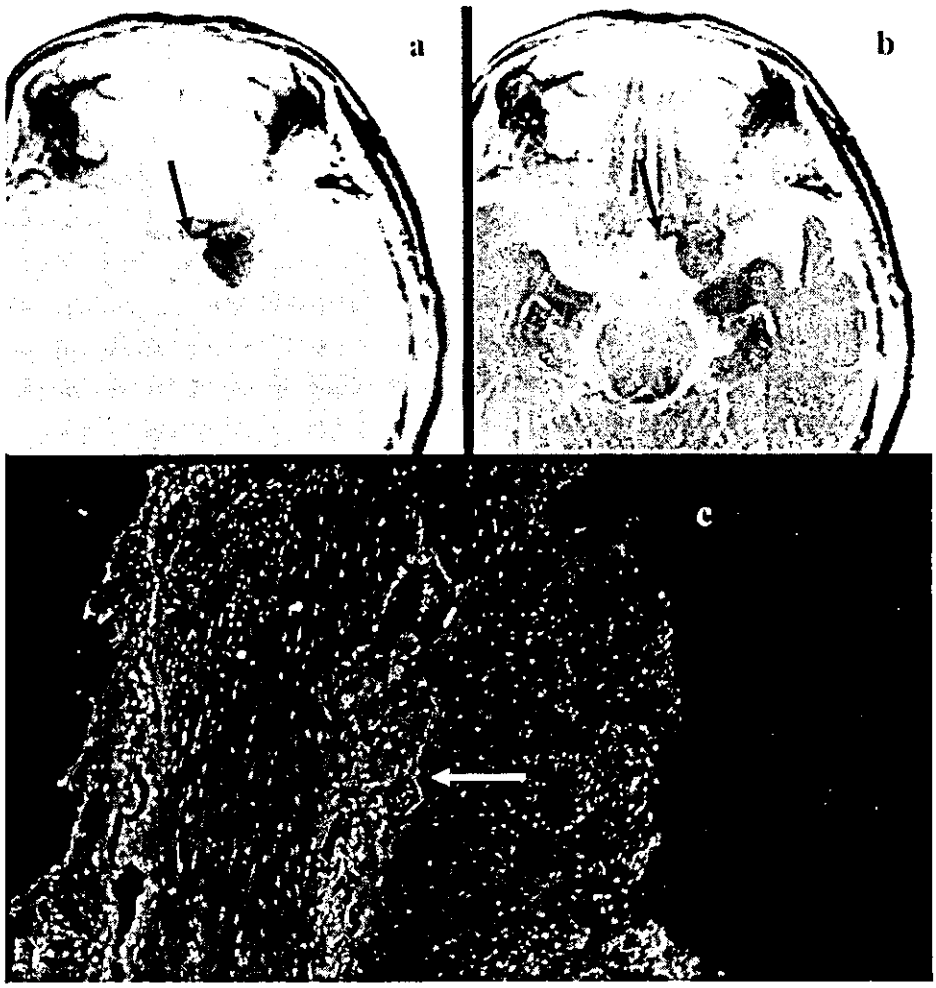

Fig. 3a–c A 72-year-old woman with a left anterior clinoid process meningioma. **a** A dural tail tapers away from the point of attachment of the tumour to the dura mater (*arrow*). **b** Its signal intensity on FLAIR images is markedly higher than that of the tumour parenchyma (*arrow*). **c** A photomicrograph shows no invasion by tumour cells, but dilated vessels in the dural tail (*arrow*)

Table 4 Relationship between the dural tail sign and tumour infiltration in five histologically proven cases

MRI characteristic	Infiltration	No infiltration
Contrast enhancement		
Weak	0	0
Equal	2	0
Moderately increased	1	0
Markedly increased	1	1
Signal on FLAIR		
Low	0	0
Isointense	3	0
Slightly increased	1	0
Markedly increased	0	1

ventricles. Initially, a long imaging time was required, but this problem was solved by applying the fast spin-echo (SE) technique. Macro et al. [17] suggested that the fast FLAIR technique be used as an adjunct to dual-echo fast SE images, especially for small or cortical lesions. On FLAIR images, meningiomas give higher signal than brain [18]. We expected that the dural tail would be detectable on FLAIR images and identified thickening of the dura mater and abnormal signal in all the regions where a dural tail was observed on contrast-enhanced T1-weighted images. It was not difficult to seen the dural tail, as we have already shown that meningiomas give higher signal than brain parenchyma [18], and the dural tail gives similar to or higher than that of the rest of the tumour. We thus found FLAIR imaging useful for showing dural abnormalities associated with meningioma without contrast medium. Among patients screened using FLAIR imaging (excluded from this study because contrast enhanced T1-weighted images were not obtained), we detected a small meningioma showing clear thickening of the dura mater and abnormal signal on FLAIR but not on T2-weighted TSE images (Fig. 4). Contrast-enhanced MRI is not often used for screening of the brain, but failure of detection of small meningiomas may be considerably reduced by using FLAIR.

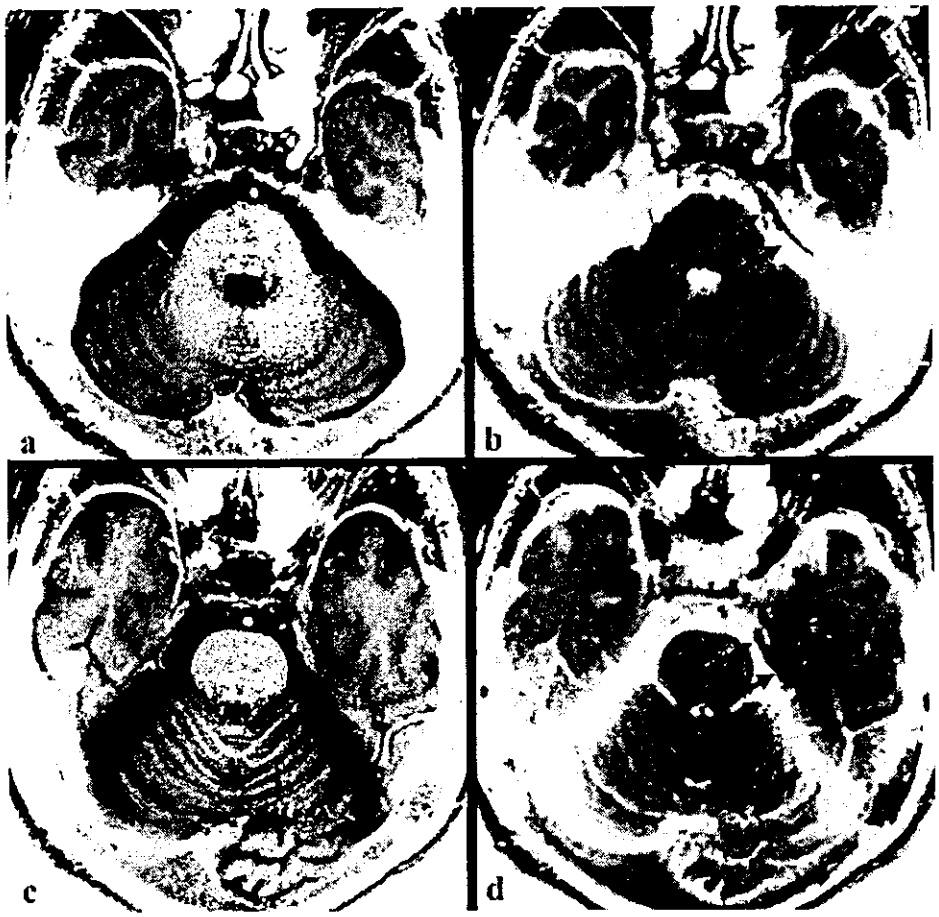

Fig. 4a–d A small meningioma (*arrowhead*) showing clear thickening of the dura mater and abnormal high signal on **b, d** FLAIR (*long arrows*), but not on **a, c** T2-weighted turbo spin-echo images

Wilms et al. [19] reported that thickening of the dura mater with marked enhancement represented neoplastic infiltration in or on the surface of the dura mater in three cases, and described the dural tail as indicating tumour infiltration. However, Tokumaru et al. [9] reported histological examination of the enhancing meninges adjacent to four meningiomas, showing only increased loose connective tissue, hypervascularity and dilated vessels. In this study, one patient showed these latter changes, and four dural infiltration. In these four patients the area corresponding to the dural tail on FLAIR was isointense with or gave slightly higher signal than the main tumour. In three of them the dural tail showed equal or moderately higher enhancement that the parenchyma of the tumour, and in the other it enhanced strongly. In the patient without tumour infiltration, the signal of the dural tail was very high on the contrast-enhanced T1-weighted and FLAIR images (Fig. 2); histology showed vascular dilatation, as in other studies. There have been no studies of infiltration of the dura mater using differences in the degree of enhancement of the dural tail. We had too few patients to assess this, but it our findings raise the question of considering of infiltration of tumour cells if the signal from the dural tail is similar to that of the tumour on FLAIR images. A dural tail showing higher signal than the tumour may suggest reactive change.

References

1. Gupta S, Gupta RK, Banerjee D, Gujral RB (1993) Problems with the "dural tail" sign. Neuroradiology 35: 541–542
2. Kutcher TJ, Brown DC, Maurer PK, Ghaed VN (1991) Dural tail adjacent to acoustic neuroma: MR features. J Comput Assist Tomogr 15: 669–670
3. Tien RD, Yang PJ, Chu PK (1991) "Dural tail sign": a specific MR sign for meningioma? J Comput Assist Tomogr 15: 64–66
4. Senegor M (1991) Prominent meningeal "tail sign" in a patient with a metastatic tumor. Neurosurgery 29: 294–296
5. Schorner W, Schubeus P, Henkes H, Lanksch W, Felix R (1990) "Meningeal sign": a characteristic finding of meningiomas on contrast-enhanced MR images. Neuroradiology 32: 90–93
6. Aoki S, Sasaki Y, Machida T, Tanioka H (1990) Contrast-enhanced MR images in patients with meningioma: importance of enhancement of the dura adjacent to the tumor. AJNR 11: 935–938
7. Goldsher D, Litt AW, Pinto RS, Bannon KR, Kricheff, II (1990) Dural "tail" associated with meningiomas on Gd-DTPA-enhanced MR images: characteristics, differential diagnostic value, and possible implications for treatment. Radiology 176: 447–450
8. Nagele T, Petersen D, Klose U, Grodd W, Opitz H, Voigt K (1994) The "dural tail" adjacent to meningiomas studied by dynamic contrast-enhanced MRI: a comparison with histopathology. Neuroradiology 36: 303-307
9. Tokumaru A, O'Uchi T, Eguchi T, et al (1990) Prominent meningeal enhancement adjacent to meningioma on Gd-DTPA-enhanced MR images: histopathologic correlation. Radiology 175: 431–433
10. Hajnal JV, De Coene B, Lewis PD, et al (1990) High signal regions in normal white matter shown by heavily T2-weighted CSF nulled IR sequences. J Comput Assist Tomogr 16: 506–513
11. De Coene B, Hajnal JV, Gatehouse P, et al (1992) MR of the brain using fluid-attenuated inversion recovery (FLAIR) pulse sequences. AJNR 13: 1555–1564
12. Kuroiwa T, Ohta T (2000) MRI appearances mimicking the dural tail sign: a report of two cases. Neuroradiology 42:199–202
13. Morioka T, Matsushima T, Ikezaki K, et al (1993) Intracranial adenoid cystic carcinoma mimicking meningioma: report of two cases. Neuroradiology 35: 462–465
14. Good CD, Kingsley DP, Taylor WJ, Harkness WF (1997) "Dural tail" adjacent to a giant posterior cerebral artery aneurysm: case report and review of the literature. Neuroradiology 39: 577–580
15. Rydberg JN, Hammond CA, Grimm RC, et al (1994) Initial clinical experience in MR imaging of the brain with a fast fluid-attenuated inversion-recovery pulse sequence. Radiology 193: 173–180
16. Noguchi K, Ogawa T, Inugami A, Toyoshima H, Okudera T, Uemura K (1994) MR of acute subarachnoid hemorrhage: a preliminary report of fluid-attenuated inversion-recovery pulse sequences. AJNR 15: 1940–1943
17. Essig M, Hawighorst H, Schoenberg SO, et al (1998) Fast fluid-attenuated inversion-recovery (FLAIR) MRI in the assessment of intraaxial brain tumors. J Magn Reson Imaging 8: 789–798
18. Shimizu T, Miki H, Takeguchi T, Kikuchi K, Mochizuki T, Ikezoe J (2003) Usefulness of turbo-fluid-attenuated inversion-recovery (tFLAIR) sequence in diagnosing meningioma. Radiat Med 21: 55–61
19. Wilms G, Lammens M, Marchal G, et al (1989) Thickening of dura surrounding meningiomas: MR features. J Comput Assist Tomogr 13: 763–768

Annals of Nuclear Medicine Vol. 18, No. 2, 137–143, 2004

Segmented attenuation correction for myocardial SPECT

Yasuyuki TAKAHASHI,* Kenya MURASE,* Teruhito MOCHIZUKI,** Hiroshi HIGASHINO,***
Yoshifumi SUGAWARA** and Akiyoshi KINDA****

*Department of Medical Engineering, Division of Allied Health Sciences, Osaka University Graduate School of Medicine
**Department of Radiology, Ehime University School of Medicine
***Department of Radiology, Ehime Prefectural Imabari Hospital
****Toshiba Medical Systems Engineering Laboratory

Purpose: One of the main factors contributing to the accuracy of attenuation correction for SPECT imaging using transmission computed tomography (TCT) with an external gamma-ray source is the radionuclide count. To reduce deterioration of TCT images due to inadequate radionuclide counts, a correction method, segmented attenuation correction (SAC), in which TCT data are transformed into several components (segments) such as water, lungs and spine, providing a satisfactory attenuation correction map with less counts, has been developed. The purpose of this study was to examine the usefulness of SAC for myocardial SPECT with attenuation correction. *Methods:* A myocardial phantom filled with Tc-99m was scanned with a triple headed SPECT system, equipped with one cardiac fan beam collimator for TCT and two parallel hole collimators for ECT. As an external gamma-ray source for TCT, 740 MBq of Tc-99m was also used. Since Tc-99m was also used for ECT, the TCT and ECT data were acquired separately. To make radionuclide counts, the TCT data were acquired in the sequential repetition mode, in which a 3-min-rotation was repeated 7 times followed by a 10-min-rotation 4 times (a total of 61 minutes). The TCT data were reconstructed by adding some of these rotations to make TCT maps with various radionuclide counts. Three types of SAC were used: (a) 1-segment SAC in which the body structure was regarded as water, (b) 2-segment SAC, in which the body structure was regarded as water and lungs, and (c) 3-segment SAC, in which the body structure was regarded as water, lungs and spine. We compared corrected images obtained with non-segmentation methods, and with 1- to 3-segment SACs. We also investigated the influence of radionuclide counts of TCT (3, 6, 9, 12, 15, 18, 21, 31, 41, 51, 61 min acquisition) on the accuracy of the attenuation correction. *Results:* Either 1-segment or 2-segment SAC was sufficient to correct the attenuation. When non-segmentation TCT attenuation methods were used, rotations of at least 31 minutes were required to obtain sufficiently large counts for TCT. When the 3-segment SAC was used, the minimal acquisition time for a satisfactory TCT map was 7 min. *Conclusion:* The 3-segment SAC was effective for attenuation correction, requiring fewer counts (about 1/5 of the value for non-segmentation TCT), or less radiation for TCT.

Key words: transmission computed tomography, emission computed tomography, segmented attenuation correction, myocardial SPECT

INTRODUCTION

SINCE THE PHOTON ENERGY of isotopes used for myocardial emission computed tomography (ECT) is relatively low, an accurate correction of intracorporeal attenuation is required. Attenuation correction using transmission computed tomography (TCT) with an external γ-ray source of ^{153}Gd or ^{99m}Tc has been reported to improve ECT

Received April 3, 2003, revision accepted December 17, 2003.

For reprint contact: Yasuyuki Takahashi, Ph.D., Department of Health, Health Planning Division, Ehime Prefectural Matsuyama Regional Office, 132, Kita-Mochida, Matsuyama, Ehime 790–8502, JAPAN.
E-mail: takahashi-yasuyuki@pref.ehime.jp

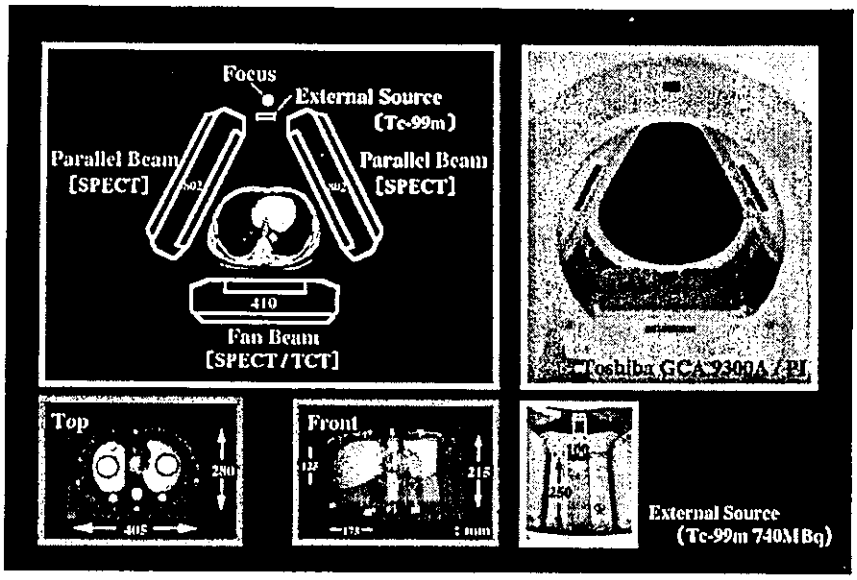

Fig. 1 The triple headed SPECT system and myocardial phantom used for TCT and ECT acquisition. The Sheet-like shape of the external γ-ray source, which was made from a bellows tube filled with 740 MBq of ^{99m}Tc, was placed at the focus of the fan beam collimator for TCT.

quantification.[1] However, the accuracy of correction using TCT images would be affected by the counts of TCT data.[2] It has been reported that an acquisition time of 15–20 min was required to obtain optimal TCT images from an external ^{99m}Tc source (1 GBq) using a gamma camera with 2 detectors.[3] Data acquisition in a shorter period of time is desirable for reducing radiation exposure and the length of restraint during examinations.

Recently, segmented attenuation correction (SAC) has been used in positron emission tomography (PET). With this method, TCT data are transformed into data maps with several segments such as air, lungs, and soft tissue. Detailed TCT data are unnecessary, and so the data acquisition time is reduced.[2–5]

In a clinical setting, an accurate attenuation-corrected myocardial image is essential for differentiating non-ischemic myocardium (uniform radionuclide counts) from ischemic myocardium (reduced radionuclide counts). In this study, we evaluated the usefulness of TCT with SAC in attenuation corrected myocardial SPECT, by examining various acquisition conditions for the SAC.

MATERIALS AND METHODS

SPECT system

The SPECT system used was a GCA-9300A/UI (Toshiba Medical Systems, Tochigi, Japan) equipped with one cardiac fan beam collimator and two parallel beam collimators. TCT data were acquired using an external gamma-ray source while myocardial ECT data were acquired using phantoms and a human subject (Fig. 1). The TCT external radiation source was a sheet-shape made from bellows tube filled with 740 MBq of ^{99m}Tc. The tube, 1 mm in inner diameter, was made of a fluorocarbon resin embedded in an acrylic rectangular board of 30 cm × 10 cm.[6] The data processor was GMS-5500A/DI (Toshiba Medical Systems, Tochigi, Japan). Both TCT and ECT images were acquired with a matrix size of 128 × 128, and a step and shoot mode (30 sec/direction) at intervals of 6 degrees (60 directions, 360-degree acquisition in total). Pixel size was 3.2 mm. Under these conditions, TCT projection counts/pixel were about 75 in the myocardial phantom and patients' myocardial area, and higher than 120 in the blank area. According to the triple-energy window (TEW) method,[7,8] the acquisition window width was set at 20% of the main window (140 keV) with a subwindow of 7%.

Fan beam TCT data were transformed to parallel beam data. Any truncation in the transformed parallel beam data was corrected using non-truncated parallel beam data.[9] An attenuation map was generated using filtered back projection (FBP). A ramp filter was used as a reconstruction filter. Butterworth filtering (cutoff = 0.31 cycle/cm, power factor = 8) was used as a post-reconstruction filter to decrease high frequency noise. ECT data of two parallel hole collimators were summed, followed by a 15 × 15-point smoothing, then reconstructed using ordered subset-expectation maximization (OSEM: Number of iterations: 10, Subsets 5)[6] with TEW scattering correction.

Description of the SAC algorithm

Three methods of segmentation were applied; SAC-1 in which the entire body outline of the myocardial phantom was regarded as water (a single peak), SAC-2, in which

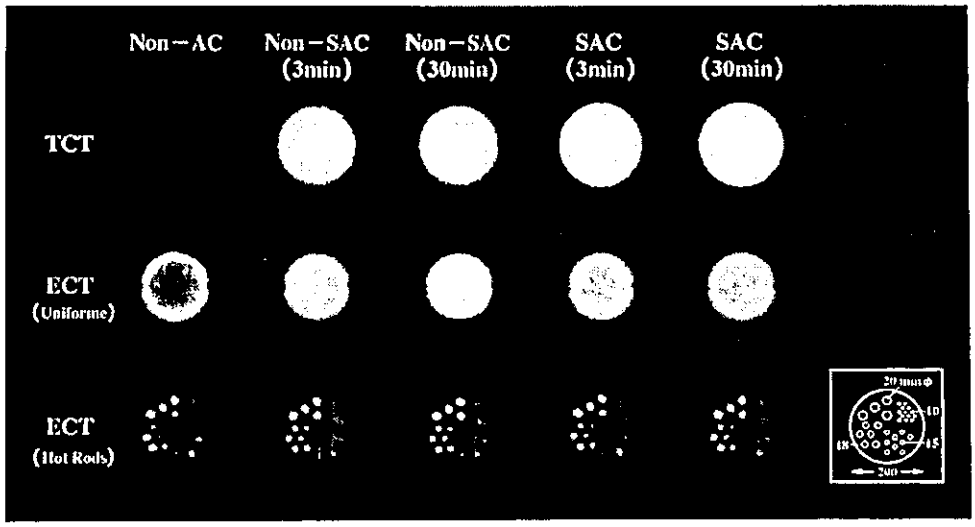

Fig. 2 The upper panel shows the attenuation image of the cylinder phantom, the middle panel the ECT image of the uniform phantom, and the lower panel the ECT image of the hot rods phantom. Images are uncorrected (Non-AC), corrected with the original TCT (Non-SAC) image (3 min or 30 min), or corrected with the SAC image (3 min or 30 min). A schema of the hot rods phantom is shown in the lower right.

the body outline was regarded as consisting of 2 peaks discriminating water and lung, and SAC-3, in which the body outline was regarded as consisting of 3 peaks discriminating water, lung and spine. A value for each segment was determined by linear transformation of coefficients of TCT map radiation attenuation using a fixed value,[3–5,10] the coefficient being 0.028/cm in lung, 0.095/cm in water, and 0.107/cm in spine.

Phantom study

The TCT data were acquired using the sequential repetition mode, in which a 3-min-rotation was repeated 7 times followed by a 10-min-rotation 4 times (a total of 61 minutes). Then, TCT-attenuation maps with various counts were generated. As a control, the best TCT-attenuation map with the highest count was produced by summing all data acquired over 61 min. ECT images were reconstructed using these TCT-attenuation maps. Approximately 100 counts/pixel were obtained from each direction in the 30-min ECT acquisition. ECT and TCT acquisition were performed in the sequential mode.[11,12] To avoid misregistration between the first (ECT) and second (TCT) images, the phantom was kept in the same position over the weekend a waiting the decay of the ECT data.

Uniform and hot rods phantoms

A cylinder phantom (200 mm in height and 200 mm in diameter, AZ-660, Anzai-Sogyo, Tokyo, Japan) was filled with 740 MBq of ^{99m}Tc. Hot rod areas (hot rods phantom) were established as shown in Figure 2. ECT images of these uniform and hot rods phantoms were generated by non-SAC (3 min, 30 min) and SAC (3 min, 30 min). ECT images without attenuation correction were also compared. To evaluate the uniformity of the ECT images, we compared the profile curves generated by the non-SAC and the SAC (Fig. 3).

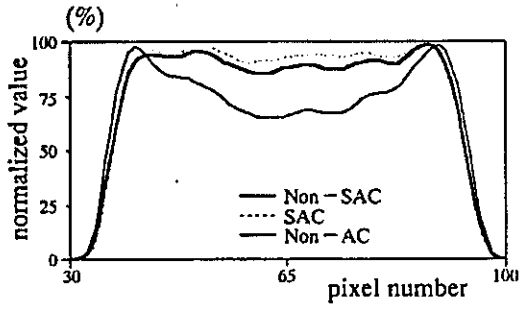

Fig. 3 Profile curves at the center of the uniform phantom. The TCT data were acquired over 30 min (Non-SAC, SAC and Non-AC).

Myocardial phantom

In a myocardial phantom with a defect (20 × 20 mm) in the anterior wall (Data Spectrum Corp., Hillsborough, NC), the myocardial compartment was filled with 92.5 kBq/m*l* of ^{99m}Tc, and the thoracic region with 9.25 kBq/m*l* of ^{99m}Tc. ECT images and Bull's eye maps were generated using TCT images of SAC-1, -2, and -3 (Fig. 4). Those without attenuation correction were also generated.

ECT images and Bull's eye maps generated by non-SAC and SAC-3 (3 and 30 min) were compared (Fig. 5).

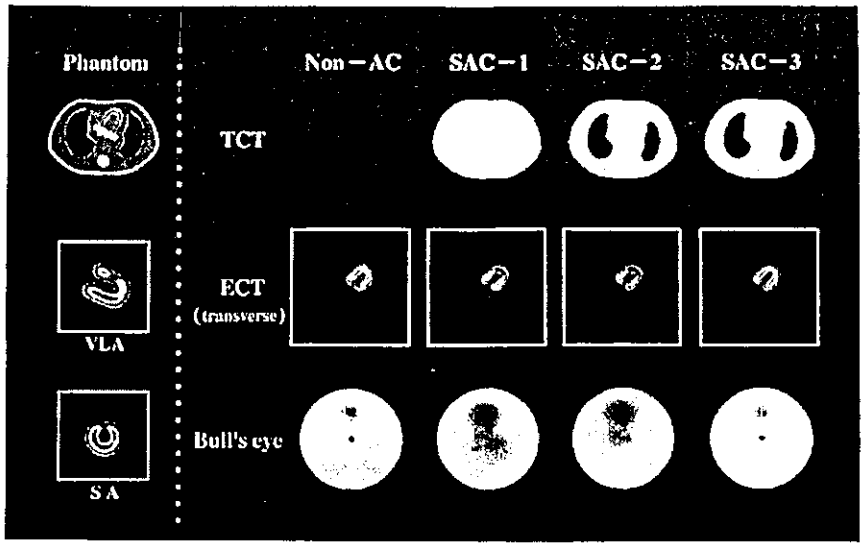

Fig. 4 Attenuation maps with each segment of the myocardial phantom (*upper row*), and SPECT images reconstructed using each map (*middle*) and the polar maps (*lower*). SAC-1 in which the entire body outline was regarded as water (a single peak). SAC-2, in which the entire body outline was regarded as consisting of 2 peaks corresponding to water and lungs. SAC-3, in which the body outline was regarded as consisting of 3 peaks corresponding to water, lungs and spine. The left side shows Non-AC. From top to bottom on the left, the myocardial phantom scheme (CT), and the myocardial images of the vertical long axis and short axis are shown. The CV of the Bull's eye maps corrected with SAC-1, -2, -3, was 24.24%, 13.92% and 3.09%, respectively. The CV without AC was 17.08%.

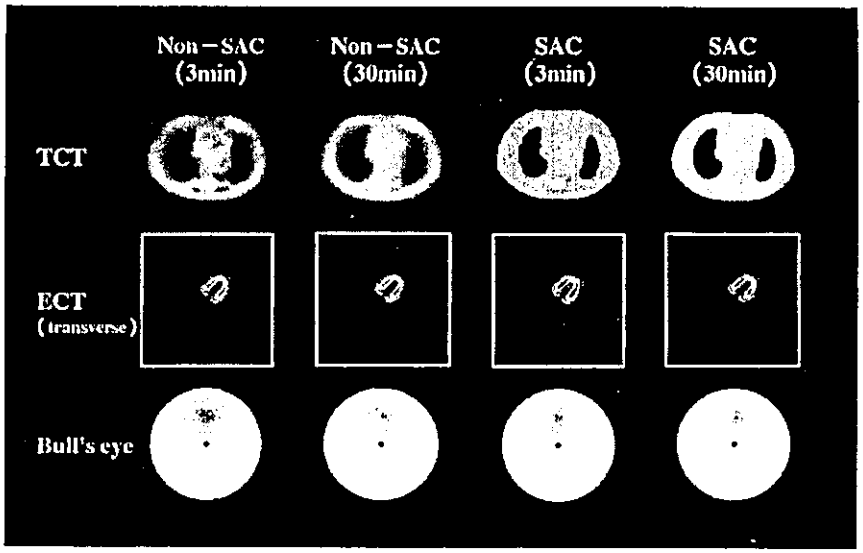

Fig. 5 The upper panel shows the attenuation maps (TCT images), the middle panel the SPECT images (ECT images), and the lower panel the polar maps (Bull's eye images) of the myocardial phantom. Images corrected with Non-SAC (3 min, 30 min) and SAC (3 min, 30 min) are shown from left to right for ECT and Bull's eye, respectively.

Human study

The human study was performed in a healthy 36-year-old male volunteer (Fig. 6). First, TCT was performed in the sequential repetition mode like in the phantom experiments (over 45 min). Immediately after TCT, 740 MBq of ^{99m}Tc-tetrofosmin was injected intravenously. Ninety

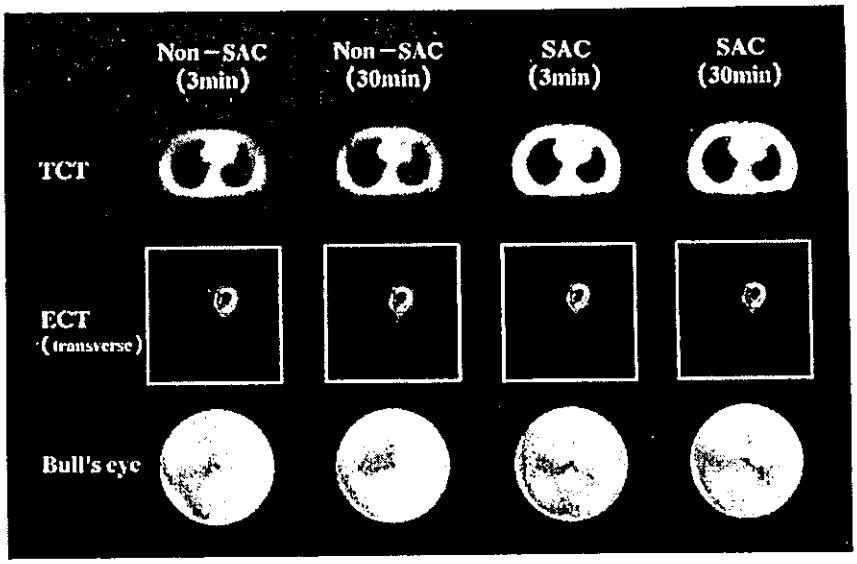

Fig. 6 The upper panel shows attenuation maps (TCT images), the middle panel SPECT images (ECT images), and the lower panel polar maps (Bull's eye images) of a human subject. Images corrected with Non-SAC (3 min, 30 min) and SAC (3 min, 30 min) are shown from left to right for ECT and Bull's eye, respectively.

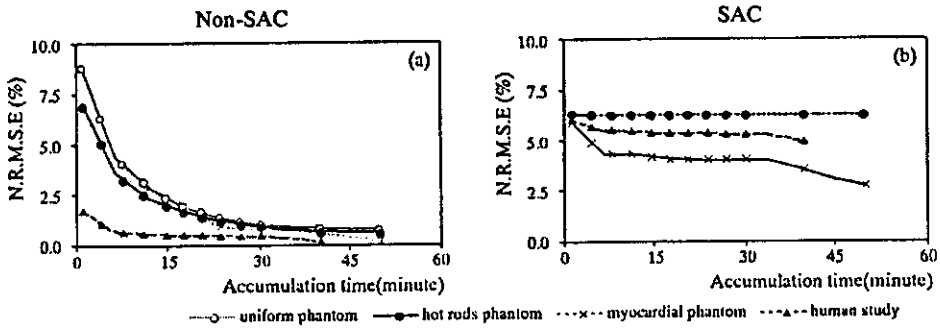

Fig. 7 Normalized root mean square errors (NRMSE) at each TCT acquisition time (Non-SAC, SAC) relative to the acquisition time for control data (61 min, Only the Human study is 41 min). (a) Non-SAC. (b) SAC.

minutes after the injection, ECT was acquired over 30 min (continuous mode). Four markers were placed on the body, and images were fused using the landmark method with an automatic registration tool (ART[13]). Images with TCT data acquired over various sampling times (3, 6, 9, 12, 15, 18, 21, 31 and 41 min) were created by summing some or all of the rotations. ECT images and Bull's eye maps generated by non-SAC and SAC-3 (3 min, 30 min) were compared (Fig. 6).

Evaluation

The uniformity in the ECT image of the cylinder phantom was expressed by a normalized mean value ± standard deviation and coefficient of variance.

For a comparison of non-SAC and SAC over acquisition time, normalized root mean square errors [NRMSE (%)] were evaluated (Fig. 7). [NRME (%):$\sqrt{[\Sigma(X_i - O_i)^2 / \Sigma O_i^2]} \times 100$: X_i: Measurement image, O_i: Standard image (non-SAC: 61 (41) min), i: pixel number ($i = 1$ n)].[14] In the evaluation of the uniform and hot rod phantoms, ECT images were used. In the myocardial phantom and human subject, Bull's eye maps were used.

RESULTS

Images and profile curves of the uniform and rods phantoms are shown in Figures 2 and 3. The normalized mean value (%) and CV (%) are 78.54 ± 15.60 and 19.86, respectively, in the images of the uniform phantom without attenuation correction (30 min). The normalized mean

value (%) and CV (%) are 92.33 ± 15.60 and 3.81 in the images of non-SAC TCT (30 min), and 95.96 ± 1.94 and 2.02, in the images of SAC TCT (30 min). The NRMSE for the rods phantom was considered.

Images of the myocardial phantom (comparison among SAC-1, -2 and -3) are shown in Figure 4. The CV of the Bull's eye maps corrected with SAC-1, -2 and -3, was 24.24%, 13.92% and 3.09%, respectively. The CV without AC was 17.08%.

Images of the myocardial phantom (comparison between Non-SAC and SAC) are shown in Figure 5. The defect area established on the anterior wall differed significantly between Non-SAC TCT and SAC-3 TCT at 30 min.

Images of the human subject are shown in Figure 6. The same tendency was observed as in the myocardial phantom.

The NRMSE of Non-SAC and SAC over acquisition time are shown in Figure 7. When Non-SAC TCT was used, NRMSE reached a plateau at about 20 min for both the uniform and hot rods phantoms (Fig. 7a). When TCT with SAC was used, NRMSE reached a plateau at about 6 min (Fig. 7b). A plateau was attained at about 20 min with Non-SAC TCT and 9 min using TCT with SAC.

In the human study, time to plateau for a satisfactory image was 9 min with Non-SAC TCT (Fig. 7a) and 6 min for TCT with SAC-3 (Fig. 7b). As shown in Figures 5 and 6, the image obtained by Non-SAC TCT (3 min, 30 min) was equivalent to that obtained by TCT with SAC-3 (3 min, 30 min).

DISCUSSION

Attenuation correction by TCT with an external source[1,11,15] or X-ray[16] is currently available in SPECT imaging reconstruction. The use of X-rays has an advantage over the use of an external source in spatial resolution (and is less influenced by the partial volume effect), resulting in a more accurate AC-map. However, the accuracy of attenuation correction depends on the image registration between the AC-map and ECT data.[17] Therefore, the AC-map generated using the X-ray CT method does not always guarantee accurate attenuation correction.[18]

On the other hand, substantial acquisition time (at least 15–20 min) is required to obtain optimal TCT images using an external source (^{99m}Tc of 1 GBq). Although data acquisition in a shorter time is desirable for clinical use, short-duration and count-limited TCT images have too much noise. Recently, PET studies have shown that segmented attenuation correction (SAC) is useful to reduce the acquisition time for TCT without increasing noise. Meikle et al.[3] reported that using SAC, accurate attenuation correction was achieved with an acquisition time as low as 2 min without an increase in noise in reconstructed PET images. In this study, we evaluated the feasibility of TCT with SAC both in phantom and in human cardiac SPECT.

We compared the uniformity of TCT images between the non-SAC and SAC methods. As shown in Figure 2, uniformity without SAC depended on the duration of the acquisition time and seemed to require approximately 20 min (i.e., the NRMSE reached a plateau at approximately 20 min, Fig. 7a) to obtain accurate and stable TCT images. On the other hand, the NMRSE remained constant in the ECT images obtained using SAC (Fig. 7b). The uniformity of ECT images using SAC was relatively independent of the data acquisition time. Indeed, visually there was little difference in either the SPECT or Bull's eye images, as shown in Figures 5 and 6. Thus, the shorter acquisition time achieved using SAC would reduce the dose or radiation to the patient.

As shown in Figure 4, the ECT images of the myocardial phantom corrected using the TCT image obtained with SAC-1 and SAC-2, were sub optimal when compared to the ECT images corrected with TCT using SAC-3. Similar results were previously reported in PET studies.

However, with SAC of a fixed value,[3–5,10] depending on the number of segments, the value from which the present weak coefficient differs varies. Therefore, if one averages the count, there is a danger of affecting the attenuation value. From this study, although SAC-3 was of the same grade as Non-SAC (original) TCT and gave a comparatively good result, it is necessary to examine dividing a segment in detail further.

CONCLUSION

The 1-segment SAC and 2-segment SAC were insufficient for attenuation correction in human myocardial SPECT. The 3-segment SAC was effective for attenuation correction, requiring fewer counts (about 1/5 of the value for non-segmentation TCT) or less radiation dose.

ACKNOWLEDGMENTS

The authors thank Mr. Kenzo Ide, Mr. Shingo Izawa and Mr. Ryousuke Ueda (Nihon Medi-Physics Co., Ltd.) for technical support.

REFERENCES

1. Van Laere K, Koole M, Kauppinen T, Monsieurs M, Bouwens L, Dierck R. Nonuniform transmission in brain SPECT using ^{201}Tl, ^{153}Gd, and ^{99m}Tc static line sources: Anthropomorphic dosimetry studies and influence on brain quantification. *J Nucl Med* 2000; 41: 2051–2062.
2. Meikle SR, Bailey DL, Hooper PK, Eberl S, Hutton BF, Jones WF, et al. Simultaneous emission and transmission measurements for attenuation correction in whole-body PET. *J Nucl Med* 1995; 36: 1680–1688.
3. Meikle SR, Dahlbom M, Cherry SR. Attenuation correction using count-limited transmission data in positron emission

tomography. *J Nucl Med* 1993; 34: 143–150.
4. Xu M, Luk WK, Cutler PD, Digby WM. Local threshold for segmented attenuation correction of PET imaging of the thorax. *IEEE Trans Nucl Sci* 1994; 41: 1532–1537.
5. Xu M, Cutler P, Luk WK. Adaptive segmented attenuation correction for whole-body PET imaging. *IEEE Trans Nucl Sci* 1996; 43: 331–336.
6. Takahashi T, Murase K, Higashino H, Sogabe I, Sakamoto K. Receiver operating characteristic (ROC) analysis of image reconstructed with iterative expectation maximization algorithms. *Ann Nucl Med* 2001; 15: 521–525.
7. Ogawa K. Simulation study of triple-energy-window scatter correction in combined Tl-201, Tc-99m SPECT. *Ann Nucl Med* 1995; 8: 277–281.
8. Ichihara T, Motomura N, Ogawa K, Hasegawa H, Hashimoto J, Kubo A. Evaluation of SPET quantification of simultaneous emission and transmission imaging of the brain using a multidetector SPET system with the TEW scatter compensation method and fan-beam collimation. *Eur J Nucl Med* 1996; 23: 1292–1299.
9. Motomura N, Ichihara T, Takayama T, Nishihara K, Inouye T, Kataoka T, et al. Practical method for reducing truncation artifacts in a fan beam transmission CT system. *J Nucl Med* 1998; 39: 178. (abstract)
10. Takahashi Y, Higashino H, Sogabe I, Sakamoto K, Murase K, Motomura N. Segmented attenuation correction by phantom experiment. *KAKU IGAKU (Jpn J Nucl Med)* 2000; 5: 250. (abstract)
11. Murase K, Tanada S, Inoue T, Sugawara Y, Hamamoto K. Improvement of brain single photon emission tomography (SPET) using transmission data acqusition in a four-head SPET scanner. *Eur J Nucl Med* 1993; 20: 32–38.
12. Stone CD, McCormick JW, Gilland DR. Effect of registration errors between transmission and emission scans on a SPECT system using sequential scanning. *J Nucl Med* 1998; 39: 365–373.
13. Ardekani BA, Braun M, Hutton BF, Kanno I, Iida H. A fully automatic multimodality image registration algorithm. *J Comput Assist Tomogr* 1995; 19: 615–623.
14. Takahashi Y, Murase K, Higashino H, Mochizuki T, Motomura N. Attenuation correction of myocardial SPECT images with X-ray CT: Effects of registration errors between X-ray CT and SPECT. *Ann Nucl Med* 2002; 16: 431–435.
15. Hashimoto J, Ogawa K, Kubo A, Ichihara T, Motomura N, Takayama T. Application of transmission scan-based attenuation compensation to scatter-corrected thallium-201 myocardial single-photon emission tomographic images. *Eur J Nucl Med* 1998; 25: 120–127.
16. Bocher M, Balan A, Krausz Y, Shrem Y, Lonn A, Wilk M, et al. Gamma camera-mounted anatomical X-ray tomography: technology, system characteristics and first images. *Eur J Nucl Med* 2000; 27: 619–627.
17. Murase K, Tanada S, Inoue T, et al. Effect of misalignment between transmission and emission scans on SPECT images. *J Nucl Med Technol* 1993; 21: 152–156.

Heterogeneity of cerebral blood flow in frontotemporal lobar degeneration and Alzheimer's disease

Michinobu Nagao[1], Yoshifumi Sugawara[2], Manabu Ikeda[3], Ryuji Fukuhara[3], Kazuhiko Hokoishi[3], Kenya Murase[4], Teruhito Mochizuki[2], Hitoshi Miki[2], Takanori Kikuchi[2]

[1] Department of Radiology, Matsuyama Medical Center for Cancer and Cardiovascular Disease, Matsuyama-City, Ehime, Japan
[2] Department of Radiology, Ehime University Medical School, Ehime, Japan
[3] Department of Neuropsychiatry, Ehime University Medical School, Ehime, Japan
[4] Department of Medical Engineering Division of Allied Health Sciences, Osaka University Medical School, Osaka, Japan

Received: 3 June 2003 / Accepted: 28 August 2003 / Published online: 15 November 2003

Abstract. This study was designed to quantify the heterogeneity on cerebral blood flow single-photon emission tomography (SPET) images in frontotemporal lobar degeneration (FTLD) and Alzheimer's disease (AD) using a three-dimensional fractal analysis. Twenty-one FTLD patients, 21 AD patients and 11 healthy controls underwent technetium-99m hexamethylpropylene amine oxime SPET scanning. Patients with FTLD and AD matched for sex, age and the severity of dementia as estimated with the Clinical Dementia Rating and were determined to be in the early stage of illness. We delineated the SPET images using a 35% cut-off and a 50% cut-off of the maximal voxel radioactivity and measured the number of voxels included in the contours of two different cut-offs. The fractal dimension (FD) was calculated by relating the logarithms of the cut-offs and the numbers of voxels, and it was defined as the heterogeneity of the cerebral perfusion. We divided the SPET images into two sets, anterior and posterior, with equal numbers of coronal SPET slices. We calculated total FD, anterior FD and posterior FD for total, anterior and posterior SPET images. Anterior FDs for FTLD and AD were 1.55±0.34 and 1.24±0.19 (P=0.0002). The ratios of anterior to posterior FD for FTLD and AD were 1.81±0.41 and 1.32±0.14 (P<0.0001). Use of the anterior FD and the ratio of anterior to posterior FD separated FTLD patients from AD patients and controls with a sensitivity of 85.7% and a specificity of 93.8%. Anterior FD and the ratio of anterior to posterior FD may be useful in distinguishing FTLD from AD.

Michinobu Nagao (✉)
Department of Radiology,
Matsuyama Medical Center for Cancer
and Cardiovascular Disease,
Yanaimachi 2-85, 790-0014 Matsuyama-City,
Ehime, Japan
e-mail: minagao@ehime.med.or.jp
Tel.: +81-89-9157701, Fax: +81-89-9157711

Keywords: Frontotemporal lobar degeneration – Alzheimer's disease – SPET – Fractal analysis

Eur J Nucl Med Mol Imaging (2004) 31:162–168
DOI 10.1007/s00259-003-1343-6

Introduction

Frontotemporal lobar degeneration (FTLD) is a non-Alzheimer's disease type of degenerative dementia characterised by a peculiar behavioural disorder, with changes in personality and social conduct due to frontotemporal involvement [1, 2]. This disorder is important and is probably the second most frequent cause of degenerative dementia [3, 4]. A pattern of frontally reduced regional cerebral blood flow (CBF) is characteristic for, but not specific to, FTLD [5, 6]. Some findings indicate that patients with features clinically corresponding to FTLD may not demonstrate the typical cerebral perfusion pattern previously described [7].

CBF single-photon emission tomography (SPET) and positron emission tomography (PET) topographical techniques have revealed that the frontal region of the brain, in addition to the parietal and temporal lobes, shows reduced CBF in patients with Alzheimer's disease (AD) at an early stage [8, 9]. Variable patterns of CBF abnormalities in AD have also been reported [10, 11, 12]. Early diagnosis is of particular importance in sociopsychological guidance and counselling, given the different clinical presentation and prognosis of FTLD and AD [13]. Although CBF SPET is widely available and offers a sensitive diagnostic tool for the assessment of regional CBF in degenerative dementia, the ability to recognise regional CBF reduction by visual interpretation is highly dependent on the quality of SPET images and the observers' level of experience [14]. To reduce inter-observer

variability in the evaluation of brain SPET studies and to allow for a more accurate assessment of the extent and severity of regional CBF abnormalities, observer-independent analysis and objective measurement of SPET perfusion abnormalities are necessary.

Differential patterns of regional CBF abnormality in degenerative dementia have been studied by SPET and PET topographical techniques [8, 9, 15]. However, an investigation focussing on the heterogeneity on CBF SPET is lacking. We hypothesise that the heterogeneous distribution on CBF SPET images may be related to disease severity and disease specificity in degenerative dementia. In this study, three-dimensional fractal analysis (3D-FA) was based on use of an intensity threshold at different cut-offs for the involved area [16]. We quantified the heterogeneity on CBF SPET images in degenerative dementia using 3D-FA and examined the usefulness of the quantification for distinguishing FTLD from AD.

Materials and methods

All procedures used in this study were performed strictly according to the clinical study guidelines of the ethics committee of our institution and were approved by the internal review board. After a complete description of the study had been provided to all participants and their relatives, written informed consent was obtained.

Subject selection

Patients with FTLD. Twenty-one consecutive out-patients with a diagnosis of FTLD were selected from the data file of the Higher Brain Function Clinic for Outpatients of the University Hospital of Ehime, University School of Medicine, between October 1998 and March 2002 [17]. Primary degenerative dementia patients who satisfied Diagnostic and Statistical Manual of Mental Disorders, third edition (DSM-III) criteria for dementia were recruited for this study. FTLD was diagnosed clinically using the consensus criteria previously proposed [1]. The patients underwent laboratory blood tests including vitamin B_{12}, thyroid function, electroencephalography, and standard neuropsychological examinations, including Mini-Mental State Examination (MMSE) [18], Alzheimer Disease Assessment Scale (ADAS) [19] and the Clinical Dementia Rating (CDR) [20]. The exclusion criteria were (a) the clinical features described as excluding FTLD by Neary et al. [1], and (b) an advanced stage of FTLD, with severe deficits or behavioural disorders that could have made assessment difficult. Patients with magnetic resonance (MR) imaging evidence of focal brain lesions and MR angiographic evidence of occlusive lesions in the cervical and intracranial arteries were also excluded.

The mean age (±SD) of the 14 women and seven men in the FTLD group was 65.5±6.2 years. The duration of illness was 2.2±1.0 years. The FTLD group contained eight patients with a Clinical Dementia Rating (CDR) of 0.5 and 13 with a CDR of 1. The MMSE score was 23.2±5.4, and the ADAS score was 13.7±5.0. According to the Lund and Manchester Groups [1], two types of histological change (i.e. Pick type and frontal lobe degeneration with or without motor neurone disease) underlie the atrophy and share an identical anatomical distribution in the frontal and temporal lobes. In this study, MR imaging revealed no noticeable cerebral atrophy (frontal lobe degeneration type) in six patients in the FTLD group, while striking circumscribed atrophy in the frontal and anterior temporal lobes (Pick type) was observed in 15.

Patients with AD. Twenty-one patients (13 women and 8 men) with probable AD were randomly sampled from the same data file of the Higher Brain Function Clinic for Outpatients of the University Hospital and were matched for sex, age, duration of dementia and severity of dementia as estimated with the CDR. The clinical diagnosis of probable AD was based on the National Institute of Neurological and Communicative Disorders/Stroke and Alzheimer's Disease and Related Disorders Association (NINCDS/ADRDA) criteria [21]. All patients had a history of gradually progressive intellectual deterioration without focal motor or sensory signs. The patients with a CDR of 0.5 ("very mild" cases) were only included in the analysis when they fulfilled the clinical criteria for probable AD in a subsequent clinical follow-up.

All patients in the AD group underwent examinations similar to those undergone by the FTLD group. Their mean age (±SD) was 69.6±6.9 years, and the duration of illness was 2.0±0.5 years. The AD group contained seven patients with a CDR of 0.5 and 14 with a CDR of 1. The MMSE score was 21.6±4.6, and the ADAS score was 14.2±4.7. Brain MR images with AD patients showed no remarkable cerebral atrophy.

Healthy control subjects. Eleven healthy controls (seven women and four men) with normal cognitive findings were recruited from the community. Control and patient groups were matched for sex and age. Normal physical and neurological examination results were obtained in all control subjects, none of whom had a history of psychiatric or neurological disorders. No abnormal findings were seen on MR images in these subjects, and all scored 28 or higher on the MMSE. Their age was 65.6±6.6 years.

Data acquisition

Hexamethylpropylene amine oxime (HMPAO) was labelled with technetium-99m on site shortly before administration. The dose was approximately 740 MBq. The radiopharmaceutical was injected into an antecubital vein while the subject lay in a supine position with the eyes closed in a secluded examination room. SPET was performed 5 min after the injection. A SPET scanner (SPECT-2000H; Hitachi Medical Corp., Tokyo, Japan) incorporating a four-headed rotating gamma camera with an in-plane and axial resolution of 7.5 mm full-width at half-maximum (FWHM), and equipped with low-energy high-resolution collimators, was used for scanning. Data were obtained by using the 140-keV photopeak (20% window) over 360° rotation and a 128×128 matrix. The step and shoot format was utilised with an acquisition time of 20 s/step. Image reconstruction was performed by the filtered back-projection method using a Butterworth filter as a preprocessing filter (order 10, cut-off frequency 0.12 cycles/pixel). Attenuation correction was performed using Chang's method by assuming the object shape to be an ellipse for each slice and the attenuation coefficient to be uniform (0.08 cm^{-1}). The pixel size in the reconstructed images was 2 mm×2 mm×2 mm. Slice thickness of SPET images was 2 mm (Fig. 1).

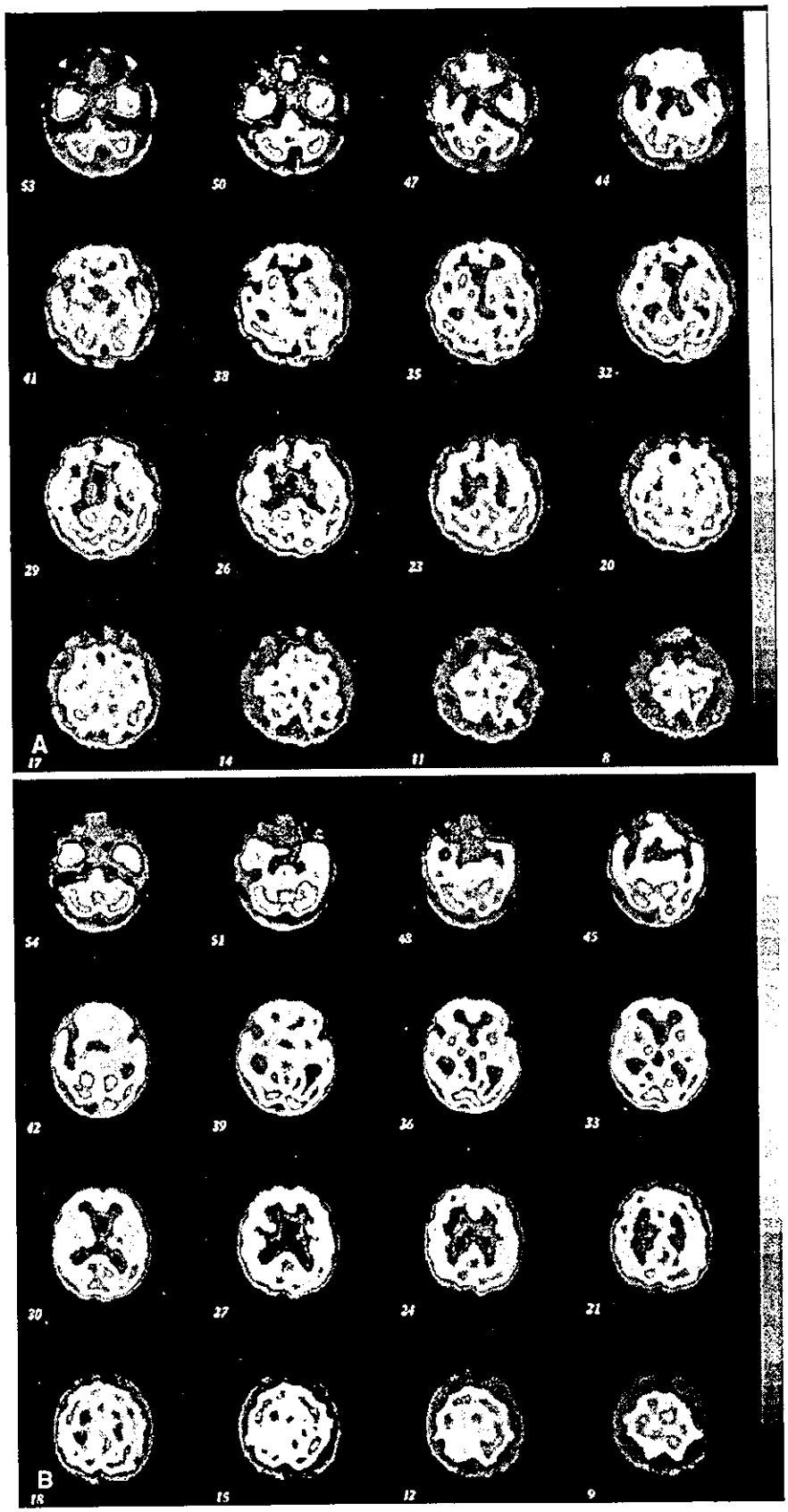

Fig. 1. A SPET images for a 62-year-old male with FTLD, showing bifrontal hypoperfusion more evident on the right than on the left. His total FD, anterior FD and posterior FD were 1.30, 1.47 and 1.08. B SPET images for a 65-year-old male with AD, showing right parieto-occipital hypoperfusion with slight involvement of both frontal lobes. His total FD, anterior FD and posterior FD were 1.13, 1.34 and 0.93

Three-dimensional fractal analysis

Fractals have been introduced by Mandelbrot [22] to characterise structures and processes occurring in nature. The principal features of fractal objects are: (1) a large degree of heterogeneity, (2) scaling similarity over many scales of observation and (3) the lack of a well-defined scale [23]. Strictly speaking, a structure (such as lung vasculature or vermis of the cerebellum) is fractal if its small-scale appears similar to its large-scale form. Fractal geometry is characterised by the relationship between a measure (M) and the scale (ε), expressed as:

$$M(\varepsilon) = k \cdot \varepsilon^{-D}$$

where k is a scaling constant and D is the fractal dimension [22]. As this equation implies, the quantity M to be measured is a function of the ruler scale and can be a non-constant. The fractal dimension is one parameter that is useful for this purpose in characterising organisationally complex structures [23]. The fractal dimension is a scale-independent measure of spatial or temporal heterogeneity.

In 3D-FA, the chosen cut-offs were used as the ruler scale ε in the above equation, and the number of voxels with radioactivity higher than the corresponding cut-offs were expressed as $M(\varepsilon)$. Clearly, $M(\varepsilon)$ decreases as ε increases; hence, a linear regression on the $M(\varepsilon)$ versus ε graph, when plotted on a logarithm versus a logarithm scale, yields a negative slope with the magnitude equal to the fractal dimension.

In this study, we delineated the SPET images using a 35% and a 50% cut-off of the maximal voxel radioactivity and measured the number of voxels included in the contours of two different cut-offs. The fractal dimension (FD) was calculated by relating the logarithms of the cut-offs and the numbers of voxels based on the above equation, and it was defined as the heterogeneity of cerebral perfusion [24, 25].

We divided the SPET images into two sets, anterior and posterior, with equal numbers of coronal SPET slices. We calculated total FD, anterior FD and posterior FD for total, anterior and posterior SPET images. The number of coronal SPET slices of the anterior or posterior set for FTLD, AD and the control group were 40.4±1.3 (mean±SD), 40.4±1.6 and 40.3±0.9 respectively. There was no difference in the number of SPET slices among these three groups.

Statistical analysis

One-way analysis of variance followed by the Bonferroni method of multiple comparisons was used to compare the FTLD, AD and healthy control groups. The correlations between anterior FD and posterior FD were determined using Pearson's correlation coefficient. A P value of less than 0.05 was considered statistically significant.

Results

Total FDs (mean±SD) for the FTLD, AD and control groups were, respectively, 1.17±0.18, 1.11±0.15 and 0.86±0.08 (P<0.0001 vs FTLD group, P<0.0001 vs AD group). There was no significant difference in total FD between the FTLD and AD groups (Fig. 2).

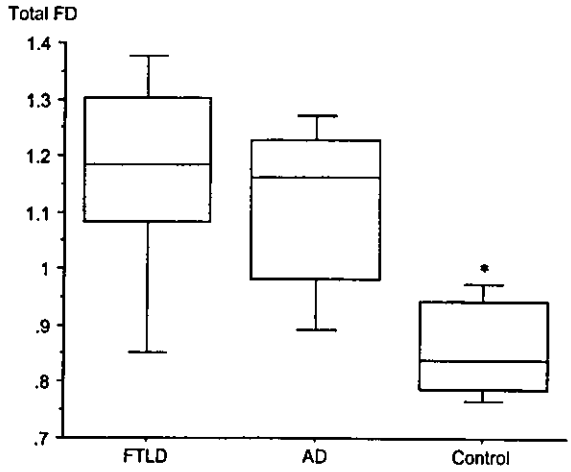

Fig. 2. Box-and-whisker plot showing the total FD for patients with FTLD, patients with AD and controls. The *boxes* represent a 25–75% range; *bisecting lines* show the median value, and *horizontal lines* represent a 10–90% range. *P<0.0001 vs FTLD group; P<0.0001 vs AD group

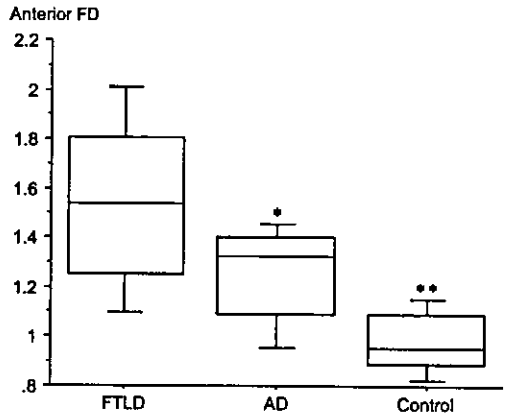

Fig. 3. Box-and-whisker plot showingthe anterior FD for patients with FTLD, patients with AD and controls. The *boxes* and *horizontal lines* are the same as in Fig. 2. *P=0.0002 vs FTLD group; **P<0.0001 vs FTLD group, P=0.009 vs AD group

Anterior FDs for the FTLD, AD and control groups were 1.55±0.34, 1.24±0.19 (P=0.0002 vs FTLD group) and 0.98±0.13 (P<0.0001 vs FTLD group, P=0.009 vs AD group) (Fig. 3).

Posterior FDs for the FTLD, AD and control groups were 0.87±0.14, 0.95±0.16 and 0.72±0.08 (P=0.007 vs FTLD group, P<0.0001 vs AD group). There was no significant difference in posterior FD between the FTLD and AD groups (Fig. 4).

The ratios of anterior FD to posterior FD for the FTLD, AD and control groups were 1.81±0.41, 1.32±0.14 (P<0.0001 vs FTLD group) and 1.37±0.20 (P=0.0002 vs FTLD group). There was no significant differ-

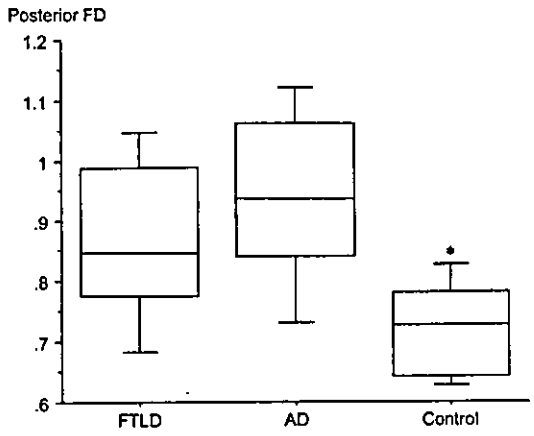

Fig. 4. Box-and-whisker plot showing the posterior FD for patients with FTLD, patients with AD and controls. The *boxes* and *horizontal lines* are the same as in Fig. 2. *P=0.007 vs FTLD group; P<0.0001 vs AD group

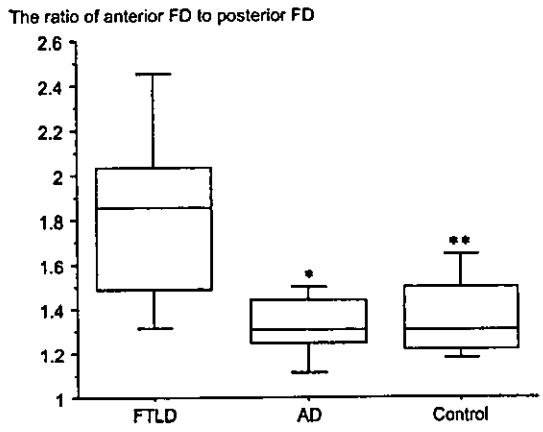

Fig. 5. Box-and-whisker plot showing the ratio of anterior FD to posterior FD for patients with FTLD, patients with AD and controls. The *boxes* and *horizontal lines* are the same as in Fig. 2. *P<0.0001 vs FTLD group; **P=0.0002 vs FTLD group

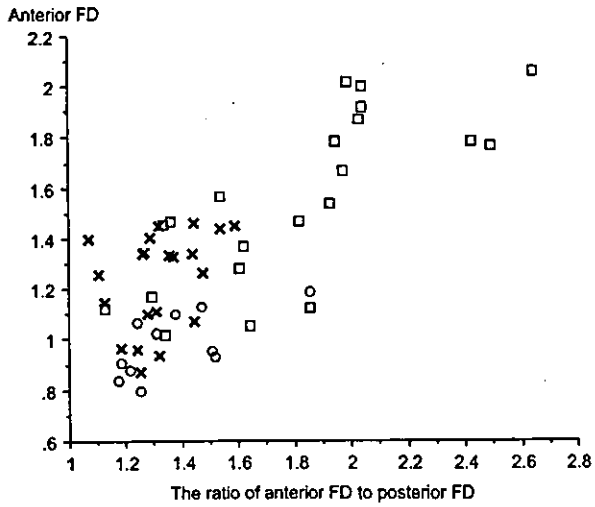

Fig. 6. Scatter plot of anterior FD and the ratio of anterior FD to posterior FD for 21 patients with FTLD (□), 21 patients with AD (×) and 11 controls (○)

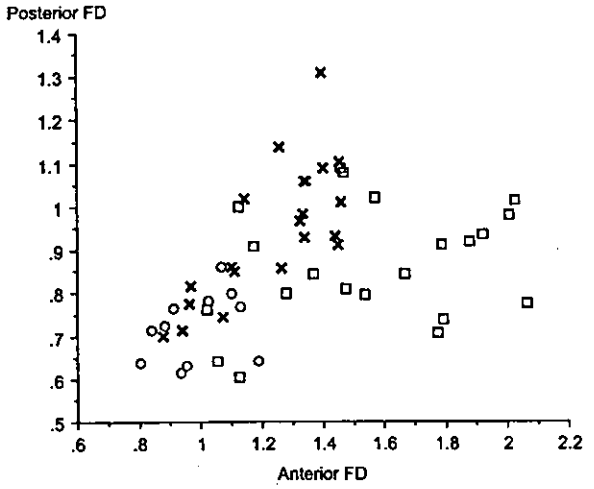

Fig. 7. Scatter plot of the relationship between anterior FD and posterior FD for 21 patients with FTLD (□), 21 patients with AD (×) and 11 controls (○). A statistically significant correlation was obtained between anterior FD and posterior FD in AD (r=0.750, P<0.0001). There was no significant correlation between the FTLD group and controls

ence in the ratio of anterior FD to posterior FD between the AD and control groups (Fig. 5).

When a patient with an anterior FD of more than 1.46 or an anterior FD to posterior FD ratio of more than 1.6 was diagnosed as having FTLD, these criteria separated FTLD patients from AD patients and controls with a sensitivity of 85.7% (18/21) and a specificity of 93.8% (30/32) (Fig. 6).

A statistically significant correlation was obtained between anterior FD and posterior FD in AD (r=0.750, P<0.0001). There was no significant correlation between anterior FD and posterior FD in the FTLD and control groups (Fig. 7).

Discussion

3D-FA allowed successful evaluation of the heterogeneous distribution on CBF SPET in patients with FTLD and AD. Anterior FD became significantly greater from

the control to the AD group and from the AD to the FTLD group (Fig. 3), while posterior FD tended to become greater from the FTLD to the AD group (Fig. 4). Due to these results, there was a more significant difference between the FTLD and the AD group in the ratio of anterior FD to posterior FD than in anterior FD (Fig. 5). Although there were many overlaps in anterior FD between the AD and the FTLD group, criteria relating to both of the aforementioned parameters (an anterior FD of more than 1.46 or an anterior FD to posterior FD ratio of more than 1.6) clearly distinguished FTLD patients from AD patients (Fig. 6). The ratio of anterior FD to posterior FD, which indicates the anterior or posterior predominance of the disease severity, may be useful for differential diagnosis of FTLD from AD.

In FTLD, the most common histological pattern consists of a severe, extensive loss of pyramidal neurones in the upper layers of the cerebral cortex of the frontotemporal area, with microvacuolation and mild superficial gliosis. There may be severe gliosis within the grey and white matter, swollen achromatic neurones, and tau- and ubiquitin-staining neuronal inclusion bodies (Pick bodies) [2, 26]. The first brain structure to be affected by progressing AD is the cerebral cortex, but in early FTLD involvement may be widespread from the cerebral cortex to the subcortical structure and basal ganglia [27, 28]. A severe loss of neurones, cortical atrophy and white matter gliosis in FTLD, which are never seen in AD, contribute to the great decrease in regional CBF. Consequently, the attenuation distribution on CBF SPET becomes more heterogeneous. Since the histological changes predominantly affect the frontal and anterior temporal lobes in FTLD, the anterior FD for patients with FTLD was significantly greater than that for patients with AD.

As shown in Fig. 7, the increase in posterior FD correlates significantly with the increase in anterior FD in AD. In AD, the laminar distributions of neurofibrillary tangles and of senile plaques suggest selective impairment of corticocortical connections [29, 30]. Parts of the brain affected in AD are tightly connected to each other, and global neurodegeneration and remote effects from severely affected areas influence the global CBF distribution [31, 32]. The association between anterior FD and posterior FD supports the morphological characteristics of corticocortical connections in AD.

However, there was no association between anterior FD and posterior FD in FTLD. Some patients with a large anterior FD in FTLD had a small posterior FD (Fig. 7). The discrepancy between anterior FD and posterior FD suggests that posterior CBF may be independent of anterior CBF abnormality in FTLD. The large anterior FD and the high ratio of anterior FD to posterior FD are findings possibly specific to FTLD.

An important factor for 3D-FA is the range of cut-off levels used. In the process of this study, we used three different cut-off ranges (35%–50%, 35%–70%, and 55%–70%) in an attempt to maximise the accuracy of 3D-FA. Significant differences in anterior FD were obtained between the AD and FTLD groups using these three cut-off ranges. The most significant difference was obtained with the 35%–50% cut-off range. In HMPAO SPET studies, when a cut-off of less than 30% is used, regions outside the brain tend to be delineated, especially in younger patients. The 35%–50% cut-off range corresponds to the change in cortical CBF whereas the 55–70% cut-off range mainly corresponds to the central brain structure. 3D-FA on CBF SPET should focus on the heterogeneity of cortical CBF because the first affected brain structure with progressing degenerative dementia is the cerebral cortex.

Fractal analysis has been applied as a diagnostic tool in SPET and PET because spatial variations in ventilation, regional blood flow and metabolism in the living organ are measurable even with low spatial resolution techniques such as PET and SPET. Kuikka et. al described the fractal analysis of two-dimensional SPET images by applying a box counting method [33, 34]. 3D-FA in the present study was based on use of an intensity threshold at different cut-offs for the involved area [16]. Since an increase in spatial heterogeneity on SPET images could indicate the presence of a region of abnormally high or low radioactivity, a varying intensity in the involved area may be related to the heterogeneous distribution. 3D-FA measures the attenuation solution or the attenuation heterogeneity in a target organ.

A statistical image analysis of CBF SPET [35] reported that 3D-FA successfully indicated a difference in the heterogeneity of CBF between vascular dementia and controls and that three-dimensional stereotactic surface projections (3D-SSP) visualised the abnormal distribution patterns in vascular dementia. 3D-FA is a simple and objective image analysis method, similar to 3D-SSP, and is a helpful tool for characterisation of CBF distribution patterns, which is not easy using conventional visual analysis. Furthermore, previous studies in patients with Alzheimer's disease and age-matched normal subjects [36, 37] have investigated the usefulness of an artificial neural network analysis in the classification of HMPAO SPET axial scans. We consider that 3D-FA employing neural networks may be suited as a means to automate diagnosis when using CBF SPET. A disadvantage of 3D-FA is the lack of anatomical specificity. However, combination of 3D-FA with an artificial neural network approach using many data for various dementias may increase the disease specificity.

In conclusion, 3D-FA indicated significant differences in heterogeneity on CBF SPET images between patients with FTLD and those with AD. Anterior FD and the ratio of anterior FD to posterior FD may offer a useful means of easily and objectively distinguishing patients with FTLD from patients with AD.

Acknowledgements. The authors wish to thank Professor Junpei Ikezoe of the Department of Radiology and Professor Hirotaka Tanabe of the Department of Neuropsychiatry at Ehime University for their continuous encouragement and valuable suggestions, and also Dr. Shozo Nakano for proofreading this manuscript.

References

1. Neary D, Snowden JS, Gustafson L, et al. Frontotemporal lobar degeneration: a consensus on clinical diagnostic criteria. *Neurology* 1998; 51:1546–1554.
2. The Lund and Manchester Groups. Clinical and neuropathological criteria for frontotemporal dementia. *J Neurol Neurosurg Psychiatry* 1994; 57:416–418.
3. Knopman DS, Mastri AR, Frey WH, Sung JH, Rustan BA. Dementia lacking distinctive histologic feature: a common non-Alzheimer degenerative dementia. *Neurology* 1990; 40: 251–256.
4. Gustafson L. Clinical picture of frontal lobe degeneration of non-Alzheimer type. *Dementia* 1993; 4:143–148.
5. Neary D, Snowden JS, Northen B, Goulding P. Dementia of the frontal lobe type. *J Neurol Neurosurg Psychiatry* 1988; 51:353–361.
6. Miller BL, Cummings JL, Villanueva-Meyer J, et al. Frontal lobe degeneration: clinical, neuropsychological, and SPECT characteristics. *Neurology* 1991; 41:1347–1382.
7. Launes J, Sulkava R, Erkinjuntti T, et al. Technetium-99m HMPAO SPECT in suspected dementia. *Nucl Med Commun* 1991; 12:757–765.
8. Minoshima S, Giordani B, Frey KA, et al. Metabolic reduction in the posterior cingulate cortex in very early Alzheimer's disease. *Ann Neurol.* 1997; 42:85–94.
9. Imran MB, Kawashima R, Awata S, et al. Parametric mapping of cerebral blood flow deficits in Alzheimer's disease: a SPECT study using HMPAO and image standardization technique. *J Nucl Med* 1999; 40:244–249.
10. Holman BL, Johnson KA, Gerada B, et al. The scintigraphic appearance of Alzheimer's disease: a prospective study using Tc-99m HMPAO SPECT. *J Nucl Med* 1992; 33:181–185.
11. Messa C, Perani D, Lucignani G, et al. High-resolution technetium-99m HMPAO SPECT in patients with probable Alzheimer's disease: comparison with fluorine-18-FDG-PET. *J Nucl Med* 1994; 35:210–216.
12. Ohnishi T, Hoshi H, Nagamachi R, et al. High-resolution SPECT to assess hippocampal perfusion in neuropsychiatric diseases. *J Nucl Med* 1995; 36:1163–1169.
13. Gustafson L. Frontal lobe degeneration of non-Alzheimer type. Clinical picture and differential diagnosis. *Arch Gerontol Geriatr* 1987; 6:209–223.
14. Holman BL, Devous MD Sr. Functional brain SPECT: the emergence of a powerful clinical method. *J Nucl Med* 1992; 33:1888–1904.
15. Pickut BA, Saerens J, Marien P, et al. Discriminative use of SPECT in frontal lobe-type dementia versus (senile) dementia of the Alzheimer's type. *J Nucl Med* 1997; 38: 929–934.
16. Nagao M, Murase K, Kikuchi T, et al. Fractal analysis of cerebral blood flow distribution in Alzheimer's disease. *J Nucl Med* 2001; 42:1446–1450.
17. Hokoishi K, Ikeda M, Maki N, et al. Frontotemporal lobar degeneration: a study in Japan. *Dement Geriatr Cogn Disord* 2001; 12:393–399.
18. Folstein MF, Folstein SE, McHugh PR. Mini-Mental State. A practical method for grading the cognitive state of patients for clinician. *J Psychiat Res* 1975; 12:189–198.
19. Rosen WG, Mohs RC, Davis KL. A new rating scale for Alzheimer's disease. *Am J Psychiatry* 1984; 141:1356–1364.
20. Morris JC. The Clinical Dementia Rating (CDR): current version and screening rules. *Neurology* 1993; 43:2412–2414.
21. McKhann G, Drachman D, Folstein M, et al. Clinical diagnosis of Alzheimer's disease: report of the NINCDS-ADRDA Work Group under the auspices of Department of Health and Human Services Task Force on Alzheimer's Disease. *Neurology* 1984; 34:939–944.
22. Mandelbrot B. How long is the coast of Britain? Statistical self-similarity and fractal dimension. *Science* 1967; 156:636–638.
23. Nelson T. Fractal physiologic complexity, scaling, and opportunities for imaging. *Invest Radiol* 1990; 25:1140–1148.
24. Chung HW, Huang YH. Fractal analysis of nuclear medicine images for the diagnosis of pulmonary emphysema: interpretations, implications, and limitations. *AJR* 2000; 174:1055–1059.
25. Nagao M, Murase K. Measurement of heterogeneous distribution on Technegas SPECT images by three-dimensional fractal analysis. *Ann Nucl Med* 2002; 16:369–376.
26. Snowden JS, Neary D, Mann DMA. *Fronto-temporal lobar degeneration: fronto-temporal dementia, progressive aphasia, sematic dementia.* New York: Livingstone, 1996.
27. Ishii K, Sakamoto S, Sasaki M, et al. Cerebral glucose metabolism in patients with frontotemporal dementia. *J Nucl Med* 1998; 39:1875–1878.
28. Kitagaki H, Mori E, Hirono N, et al. Alteration of white matter MR signal intensity in frontotemporal dementia. *Am J Neuroradiol* 1997; 18:367–378.
29. DeKosky ST, Harbaugh RE, Schmitt FA, et al. The Intraventricular Bethanecol Study Group: cortical biopsy in Alzheimer's disease: diagnostic accuracy and neurochemical, neuropathological, and cognitive correlations. *Ann Neurol* 1992; 32:625–632.
30. Meyer M, Koeppe RA, Frey KA, et al. Positron emission tomography measures of benzodiazepine binding in Alzheimer's disease. *Arch Neurol* 1995; 52:314–317.
31. Terry RD, Peck A, Deteresa R, et al. Some morphometric aspects of the brain in senile dementia of the Alzheimer type. *Ann Neurol* 1981; 10:184–192.
32. Rogers J, Morrison JH. Quantitative morphology and regional and laminar distribution of senile plaques in Alzheimer's disease. *J Neurosci* 1985; 5:2801–2808.
33. Kuikka JT, Bassingthwaighte JB, Henrich MM. Mathematical modeling in nuclear medicine. *Eur J Nucl Med* 1991; 18: 351–361.
34. Kuikka JT. Effect of tissue heterogeneity on quantification in positron emission tomography. *Eur J Nucl Med* 1995; 22: 1457–1458.
35. Yoshikawa T, Murase K, Oku N, et al. Statistical image analysis of cerebral blood flow in vascular dementia with small-vessels disease. *J Nucl Med* 2003; 44:505–511.
36. Page MP, Howard RJ, O'Brien JT, Buxton-Thomas MS, Pickering AD. Use of neural networks in brain SPECT to diagnose Alzheimer's disease. *J Nucl Med* 1996; 37:195–200.
37. Hamilton D, O'Mahony D, Coffey J, et al. Classification of mild Alzheimer's disease by artificial neural network analysis of SPET data. *Nucl Med Commun* 1997; 18:805–810.